Eruption style and dynamics of the 87 ka Baricha peralkaline rhyolite eruption in Ethiopia

Amdemichael Zafu Tadesse, Karen Fontijn, Paul A Wallace, Lucia Gurioli, Priya Laha, Herman Terryn, Dereje Ayalew

Bulletin of Volcanology (2024) 86:93
https://doi.org/10.1007/s00445-024-01787-9

RESEARCH ARTICLE

Eruption style and dynamics of the ~ 87 ka Baricha peralkaline rhyolite eruption in Ethiopia

Amdemichael Zafu Tadesse[1,2,3] · Karen Fontijn[1] · Paul A. Wallace[1,4] · Lucia Gurioli[5] · Priya Laha[6] · Herman Terryn[6] · Dereje Ayalew[3]

Received: 11 June 2024 / Accepted: 10 November 2024 / Published online: 18 November 2024

Abstract

Peralkaline rhyolites are a rare magma type, typically associated with continental rift settings, and characterised by excess alkalis relative to alumina and a moderate-low viscosity compared to calc-alkaline equivalents. Despite their prevalence in extensional rift settings, such as the Main Ethiopian Rift, eruption dynamics of peralkaline magmas are poorly understood and have never been directly observed. To address the knowledge gap, this study investigates the style and dynamics of the ~ 87 ka explosive eruption at Baricha volcano as a case study. This eruption deposited widespread pumice lapilli fall and pyroclastic density currents, which provide valuable information on pre- and syn-eruptive magmatic processes. By examining the physical and textural features of the eruption products at different stratigraphic levels, we reconstruct eruption dynamics over time. Our analysis reveals that the eruption had three distinct phases, each characterised by different types of tephra fall deposits and associated with different plume and vent conditions. Specifically, deposits of phases 1 and 3 were characterised by massive and well-sorted tephra falls indicative of sustained plume behaviour, while phase 2 deposits were bedded, lithic-rich (i.e. non-juvenile fragments) tephra falls, and pyroclastic density current deposit associated with an unsteady plume and vent-widening phase. The pumice (8–16 mm size fraction) from this eruption is microlite-free, with a bulk density of 400–700 kg m^{-3} and > 60% total vesicularity. The vesicle size distribution is polymodal, with the most frequent size ranging from 0.001 to 2.4 mm and an estimated vesicle number density of $0.07*10^7$ to $1.6*10^7$ mm^{-3}. The textural observations suggest rapid nucleation occurred during the late phases of magma ascent. Calculated decompression rates of the ascending magma were 0.07–5.6 MPa/s and show a variation between the eruption phases. We conclude that the shift in eruption dynamics alternating between steady to unsteady plume behaviour during the eruption was likely driven by changes in conduit geometry, lithic abundance of the eruptive mixture, decompression rate, and fresh magma injection.

Keywords Baricha · Explosive volcanism · Eruption dynamics · Peralkaline rhyolite · Rift volcanism

Introduction

Peralkaline rhyolites are mostly found in extensional tectonic settings, such as the Main Ethiopian Rift (MER). The MER has more than a dozen Holocene active volcanoes,

Editorial responsibility: N. Pardo

✉ Amdemichael Zafu Tadesse
amdemichael.tadesse@earth.ox.ac.uk;
amdemichaelz@gmail.com

[1] Department of Geosciences, Environment and Society, Université Libre de Bruxelles (ULB), Brussels, Belgium

[2] Department of Earth Sciences, University of Oxford, Oxford, UK

[3] School of Earth Sciences, Addis Ababa University (AAU), Addis Ababa, Ethiopia

[4] Department of Earth and Environmental Sciences, Ludwig-Maximilians-Universität München (LMU), Munich, Germany

[5] Laboratoire Magmas et Volcans, Université Clermont Auvergne, Clermont-Ferrand, France

[6] Research Group of Electrochemical and Surface Engineering, Department of Materials and Chemistry, Vrije Universiteit Brussel (VUB), Brussels, Belgium

including Baricha volcano, that have produced peralkaline lava flows, welded ignimbrites, and unwelded pyroclastic fall and density current deposits (PDCs; e.g. Bizouard and Di Paola 1978; Fontijn et al. 2018; Tadesse et al. 2019, 2022, 2023a). These magmas have an excess of alkali elements ($(Na_2O + K_2O)/Al_2O_3$) and high volatile contents (e.g. Iddon and Edmonds 2020; Tadesse et al. 2023a). The presence of alkaline and halogen elements depolymerizes the melt, resulting in lower viscosity for peralkaline magmas compared to other rhyolites of equivalent temperature, and silica and water content (e.g. Dingwell et al. 1998; Di Genova et al. 2013). The geochemical and rheological properties of these magmas significantly influence degassing efficiency (e.g. Di Genova et al. 2013), which can, in turn, affect their rheology and eruption behaviour. Thus, a comprehensive analysis of volcanic products from past eruptions is essential to better understand the eruptive dynamics of peralkaline magmas. Since no peralkaline eruption has ever been observed directly, the potential eruption dynamics associated with this peculiar magma composition are poorly understood (Hughes et al. 2017; Clarke et al. 2019).

Explosive volcanic eruptions are highly destructive events that often seemingly follow complex patterns. Some historically recorded eruptions have displayed complex variations in eruptive style (effusive-explosive) and column behaviour (steady-unsteady) during a single eruption (e.g. 1991 Pinatubo, 79 CE Vesuvius, 2008 Chaitén, 2011 Puyehue–Cordón Caulle; Polacci et al. 2001; Gurioli et al. 2005; Shea et al. 2011, 2012, 2014; Alfano et al. 2012; Castro et al. 2012; Pistolesi et al. 2015). Rhyolitic magmatic eruptions, in particular, occur infrequently, but their hazardous nature is evident from the widespread and voluminous deposits they produce (e.g. Fontijn et al. 2018; Tadesse et al. 2022). Prior to the respective 2008 and 2011 eruptions of Chaitén and Puyehue–Cordón Caulle volcanoes, explosive-effusive transitions during rhyolitic eruptions had not been directly observed yet (e.g. Castro and Dingwell 2009; Alfano et al. 2012; Pistolesi et al. 2015). Understanding of the processes that drive effusive-explosive eruption style and steady-unsteady plume transitions in rhyolitic or other magma compositions is essential to anticipate patterns of future large eruptions. Additionally, a shift in volcanic eruption styles represents different types of volcanic hazards (e.g. Gurioli et al. 2005; Pardo et al. 2014; Cioni et al. 2015; Houghton and Carey 2015).

Eruption behaviour fluctuations of a same volcano during multiple eruptions may be attributed to processes associated within magma reservoirs those play roles during eruption initiation (Cassidy et al. 2018). Processes such as new magma injection are sometimes responsible for eruption behaviour transitions (Sparks et al. 1977; Ruprecht and Bachmann 2010; Degruyter et al. 2016; Kent et al. 2023). In eruptions where the magma shows a homogenous chemical composition and initial volatile content, complex changes in eruptive style within a single eruptive episode are often linked to variations in magma flow behaviour in the conduit. These changes can result from variation in magma rheology as a response to changing concentrations of dissolved volatiles, bubbles and crystals during magma ascent (e.g. Tait et al. 1989; Gurioli et al. 2005; Houghton et al. 2010; Castro et al. 2012; Pardo et al. 2014; Pistolesi et al. 2015), or to external environmental factors such as conduit widening (e.g. Wilson et al. 1980) or external water influx (e.g. Zimanowski et al. 2015).

In this study, we investigated the eruption style and dynamics of the peralkaline rhyolite ~ 87 ka Baricha eruption. We chose this eruption because it is spatially well dispersed and well preserved. Field characteristics of this eruption were documented in earlier studies (Tadesse et al. 2022); here we add new detailed data on the stratigraphy and petrography of the deposit on samples collected from key proximal sites. The grain size, componentry and textural data are integrated to understand the magmatic processes taking place in the conduit and to reconstruct the eruption dynamics through time.

Geological background

The Bora-Baricha-Tullu Moye volcanic system is located in the central sector of the MER (Fig. 1). The system comprises both effusive and explosive eruptions that overlie Late Pleistocene ignimbrites (1.58 ± 0.2 Ma; e.g. WoldeGabriel et al. 1990). At least two caldera-forming eruptions are identified in the complex; the most recent one dated at 107.7 ± 8.8 ka (Tadesse et al. 2022). Since then, Bora-Baricha-Tullu Moye underwent at least one moderate-to-large explosive eruption per four thousand years (Tadesse et al. 2022). The volcanic system comprises post-caldera centres that can be grouped into pyroclastic centres, obsidian coulees, lava domes and maars. The major edifices are mainly silicic pyroclastic centres such as Bora, Baricha and Tullu Moye (Fig. 1; Tadesse et al. 2023a). These major edifices have experienced several explosive eruptions in the past as revealed by tephrostratigraphic reconstructions (Fontijn et al. 2018; Tadesse et al. 2022). The chemical composition of the eruptive products generally varies from comendite at Tullu Moye to pantellerite at Bora and Baricha (Bizouard and Di Paola 1978; Fontijn et al. 2018; Tadesse et al. 2022, 2023b).

The Baricha volcano is situated in the southwestern part of the Bora-Baricha-Tullu Moye volcanic system, near the southern shore of Lake Koka (Fig. 1). The volcano is covered by unwelded pumice and ash layers with subordinate silicic lava (Di Paola 1972; Fontijn et al. 2018; Tadesse et al. 2022, 2023b). A tephrostratigraphic profile, located in a deep gully 3.5 km NW of the volcano, reveals at least 9 distinct

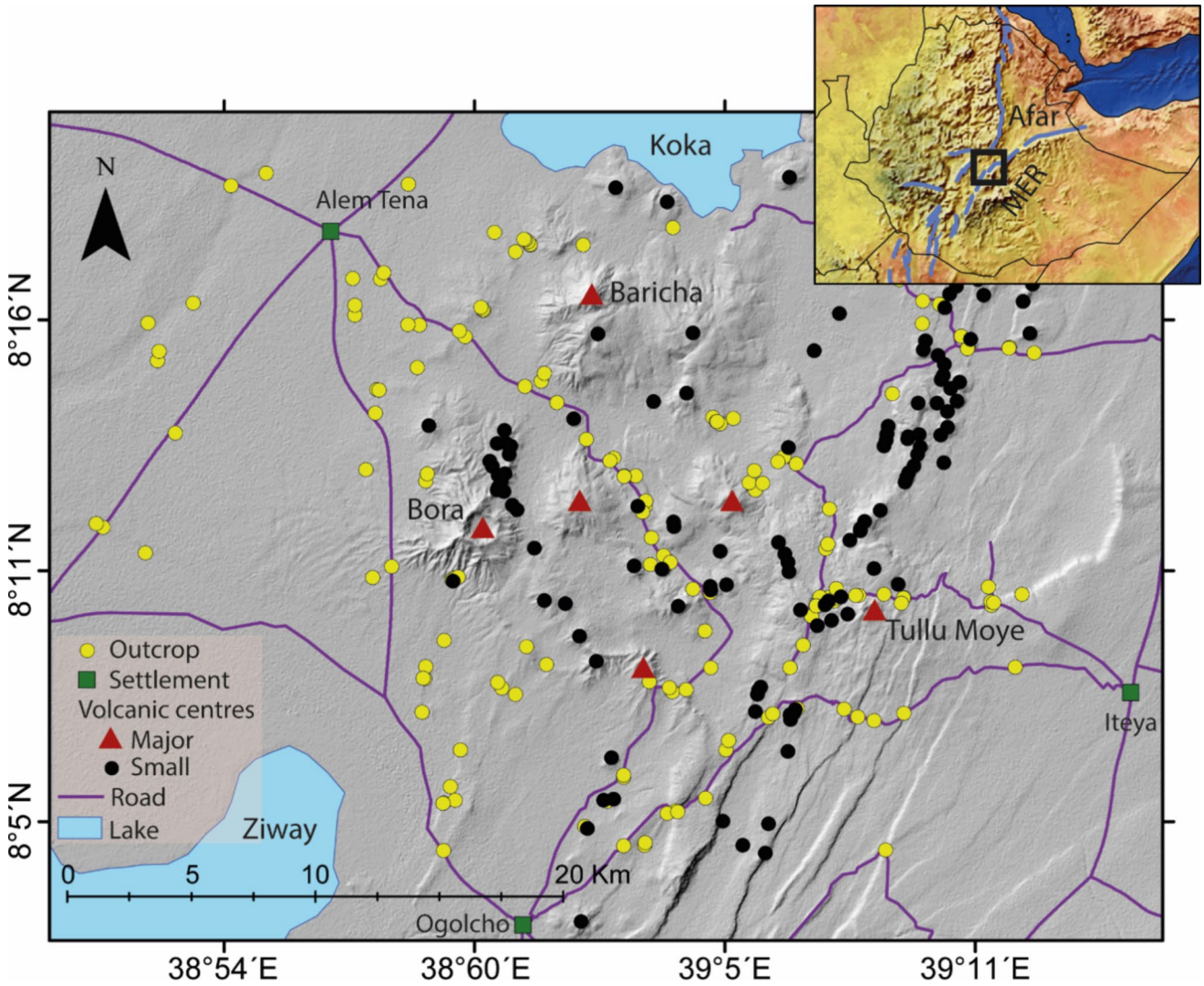

Fig. 1 Location map of the Bora-Baricha-Tullu Moye volcanic system. The map is a hillshade of 12.5 m resolution ALOS PALSAR digital elevation model (DEM) accessed from Alaska Satellite Facility (https://search.asf.alaska.edu/#/). Rectangle on the inset map shows the location of the Bora-Baricha-Tullu Moye volcanic system along the MER. Raster data set with 50 m resolution from Natural Earth Data (https://www.naturalearthdata.com/) is used on the inset map, and the MER faults (indicated by blue lines) are after Agostini et al. (2011)

explosive eruptions sourced from the vent (Fig. 2; reference location MER147 as per Fontijn et al. 2018; Tadesse et al. 2022). Those eruptions are preserved as a succession of tephra fall and PDC deposits that are separated by well-developed 5 to > 20 cm thick palaeosols, revealing variable past eruption styles. The most widely dispersed and best preserved Baricha deposit is dated at 87 ± 16 ka (Tadesse et al. 2022). The ~ 87 ka Baricha deposits are dispersed to the west with a maximum thickness of 2.7 m (i.e. MER147) and are recorded up to 20 km away from the vent with 1 m thickness (Fig. 2; Fontijn et al. 2018; Tadesse et al. 2022). A minimum bulk deposit volume of 1.3 km^3 was estimated from deposit thinning trends, equivalent to an eruption magnitude of 4.7 (Tadesse et al. 2022).

The ~ 87 ka Baricha deposit shows a stratigraphically complex sequence with variations in facies (Fig. 2; Tadesse et al. 2022). The deposit consists of three main horizons. The bottom horizon, up to 70 cm thickness, is composed of a well-sorted, massive pumice lapilli breccia. The middle horizon is 80 cm thick at the reference location (i.e. MER147), and characterised by generally well sorted and cm-to-dm-scale diffuse bedding. The middle subunit is associated with matrix-supported and poorly sorted deposits at outcrops located NW of the source vent (e.g. MER205, MER301), and which are interpreted as PDC deposits (Tadesse et al. 2022). The thickness of the PDC deposits varies from 135 cm (at 4.5 km from the vent) to 50 cm (at 8.5 km from the vent). The top 70 cm horizon of the deposit

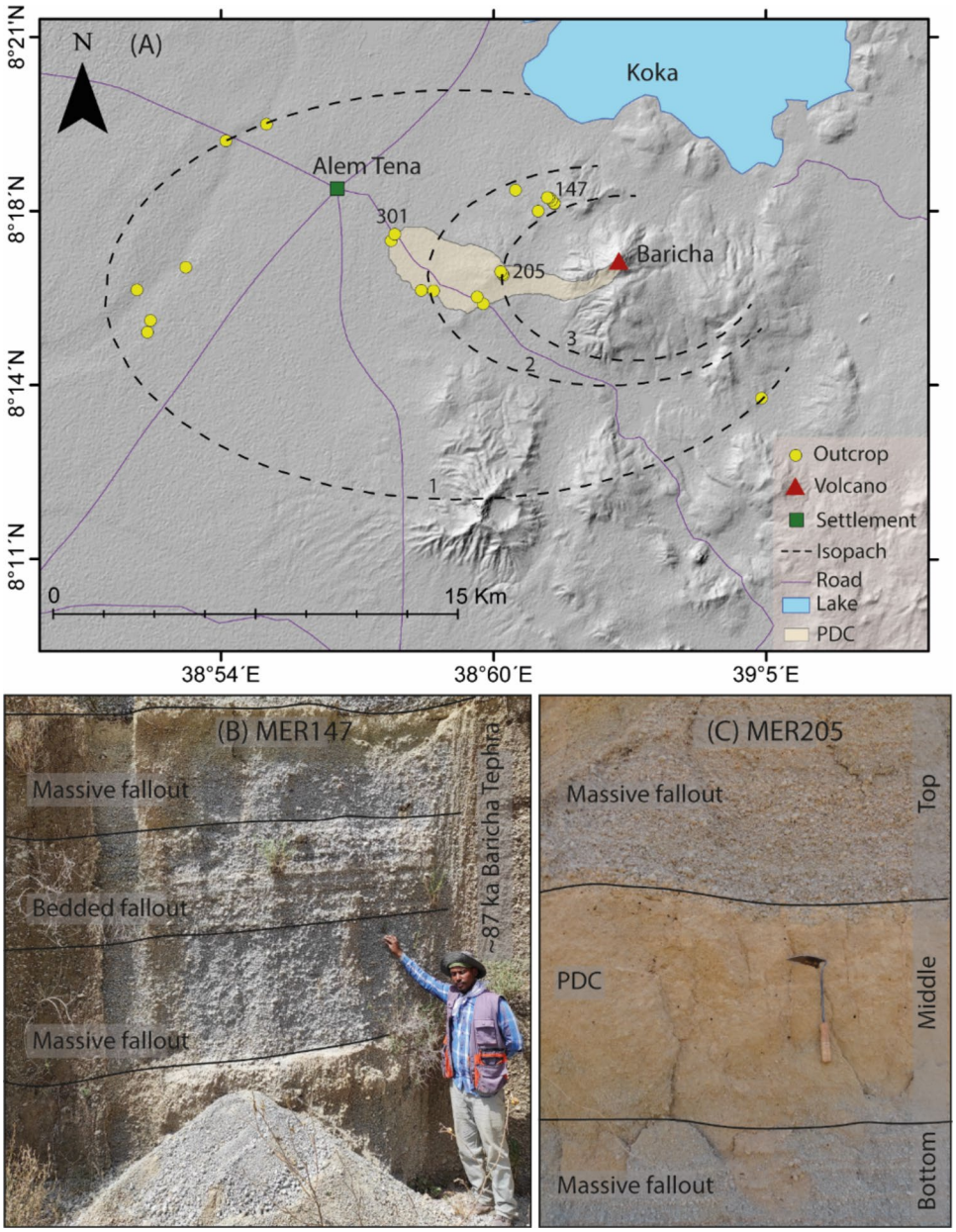

Fig. 2 **A** Isopach (thickness in meters) and pyroclastic density current (PDC) extent map of products from the ~ 87 ka Baricha eruptions (modified after Tadesse et al. 2022). The pumice clasts analysed for this study were collected at 3.5 km (MER147) and 4.5 km (MER205) from the vent, along the dispersal axis. The PDC inundation area is traced based on field observation and by following gullies. **B** and **C** Field photo of MER147 and MER205 outcrops; note that the PDC is only exposed in MER205. The section MER147 also exposes older and younger units that are separated from the ~ 87 ka Baricha tephra by palaeosols. The ~ 87 ka Baricha tephra deposit is a pumice lapilli breccia that consists of a massive horizon at the bottom-third and top-third parts, and cm-to-dm-scale diffuse bedding and associated PDC deposits in the middle part

is a pumice lapilli breccia with similar facies characteristics (i.e. well sorted, massive) to the bottom subunit. The deposit also typically shows lithic content variations along the stratigraphy, and becomes highly concentrated in lithics in the middle horizon.

At the reference location (i.e. MER147), the maximum pumice (MP) and maximum lithics (ML) clast sizes are measured in the bottom and top horizon of the deposit. The MP and ML were calculated as the geometric mean of the five largest clast dimensions measured along three perpendicular axes (Bonadonna et al. 2013). The bottom and top horizons of the deposit are both characterised by values of 4 cm for MP and 1.6 cm for ML at 3.5 km NW of the volcano.

The pumice clasts are moderately porphyritic (< 10 vol% crystals) and have a rhyolitic composition (74.4 ± 0.4 wt% SiO_2; Tadesse et al. 2022). The crystal population is mainly composed of alkali feldspar and aenigmatite, with rare Fe-Ti oxides, quartz, clinopyroxenes and amphibole. The phenocryst population is dispersed in a glassy and microlite-free groundmass (Tadesse et al. 2022). The glass major element composition is consistently pantelleritic throughout the deposit sequence, with very little to no variations in major and trace element concentrations (Figs. 3 and SI.1; Tadesse et al. 2022).

Similarly, all feldspar are sanidine and have almost the same composition at least in the bottom and top horizon of the deposit (Fig. SI.2). On the other hand, the mineral

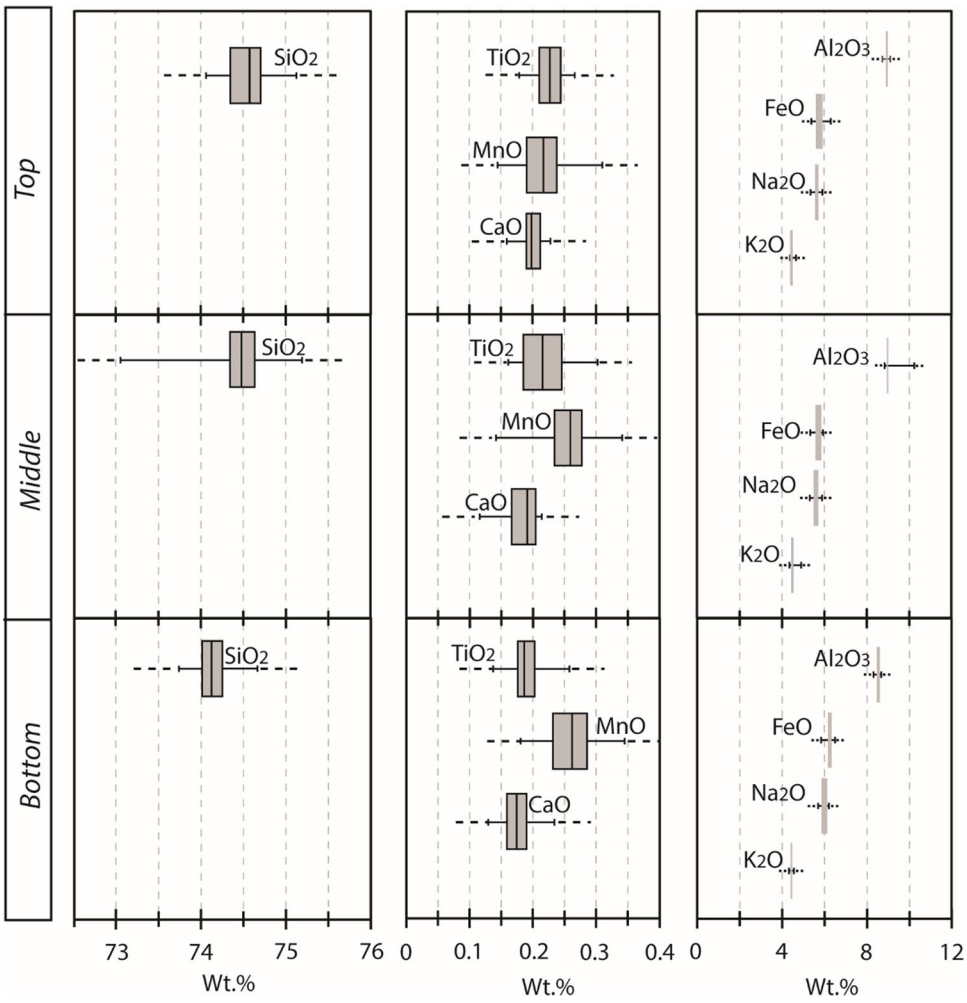

Fig. 3 Glass composition box plots of ~ 87 ka Baricha tephra at different stratigraphic level. The analytical uncertainty is indicated by dashed lines, and the presented data is from Tadesse et al. (2022). Please refer to the Appendix for the glass trace element and mineral major element composition binary plots (Figs. SI.1–4)

chemistry of amphibole and aenigmatite shows a slight variation in composition between the bottom and top horizon (Figs. SI.3 and SI.4). The amphibole minerals have two compositional clusters with Mg# (mol% (MgO)/(MgO + FeO)) ranges between < 6% and 7–10%. The amphiboles predominantly plot in the lower Mg# cluster, and only a few ($n = 11$) have higher in Mg# values and these are predominantly (but not exclusively) found in amphibole rims from the top horizon (Fig. SI.3). The aenigmatite minerals from the top stratigraphic level are generally richer in Mg, Al, Ca, and to a lesser extent in Ti than those from the bottom horizon (Fig. SI.4). Pre-eruptive water contents for the peralkaline melt as a whole was constrained to 5.1 ± 0.8 wt% from water by difference (Tadesse et al. 2023b), and this is broadly consistent with Secondary Ion Mass Spectroscopy measurements of quartz-hosted melt inclusions for other peralkaline magmas along the MER (Iddon and Edmonds 2020). Moreover, the pantelleritic magma was stored at 100 MPa pressure (~ 4 km depth) and ~ 1003 K (= 730 °C) temperature before the eruption (Tadesse et al. 2023b).

Methods

The samples for this study were collected from a stratigraphic location (i.e. MER 147) situated approximately 3.5 km northwest of Baricha volcano. The MER147 section exposes a well-preserved deposit of the ~ 87 ka Baricha eruption, which is the focus of this study. The deposit is also well-documented, supported by a robust stratigraphic reconstruction and correlation from preliminary field observations, suggesting spatial and stratigraphic variability in sedimentation behaviour and componentry (Tadesse et al. 2022). To eliminate the spatial variability and effect of wind remobilisation, we restrict our sampling to a proximal outcrop (i.e. MER147) that potentially preserves the primary variability of the juvenile components with a reduced effect from transport and depositional processes (Cioni et al. 2008; Gurioli et al. 2015). To capture stratigraphic variability, a total of ~ 6 kg tephra was collected, with ~ 2 kg channel sample from each stratigraphic horizon (i.e. base, middle, and top levels). Channel sampling is a technique usually applied to uniformly cover the overall vertical extent in the

stratigraphy during representative sample collection. This sampling strategy mainly aims to cover the entire vertical extent from top to bottom of the deposit and enables analysis of eruption characteristics at the different stages of the eruption. This sampling approach allows studying the overall variation in style during the beginning, middle and last eruption stage. Understanding the high resolution syn-eruptive temporal variations (changes at smaller time scales) would require sampling at intervals of a few cm (e.g. Gurioli et al. 2015), and is beyond the scope of this work, but recommended for future study.

The collected samples were dry-sieved at 1ϕ grain size intervals between 4ϕ (64 μm) and -5ϕ (32 mm). Each grain size fraction was weighed to construct the grain size distribution, but the finest fraction (< 64 μm), which accounts for ~ 0.07 kg of the total 2 kg sample, was excluded. Parameters such as median diameter ($Md_\phi = \phi_{50}$) and sorting ($\sigma_\phi = (\phi_{84} — \phi_{16})/2$) were calculated as per Inman (1952). Individual clasts in the coarser fractions (-5ϕ to 1ϕ) were qualitatively assigned into classes and counted. The assigned classes are pumice (vesicular juvenile), obsidian (dense juvenile), lithics (non-juvenile) and free crystals (for more details, see Tadesse et al. 2022). Up to 1600 clasts within each size fraction were counted to perform the componentry analysis, and the pumice clasts were further classified in to four categories: expanded, microvesicular, dense and tube pumice, as per Polacci et al. (2003).

Density and vesicularity analyses were carried out on > 100 randomly picked pumice clasts in the 8—16 mm grain size fraction from each stratigraphic level. A single grain size fraction was used for consistency and to avoid non-uniform grain size effects on textural parameters. Moreover, the considered grain size fraction is small enough to preserve post-fragmentation vesicle expansion (Houghton and Wilson 1989; Thomas and Sparks 1992; Tait et al. 1998). The density and total vesicularity distribution of each pumice clast was determined using a combination of gas pycnometry and an analytical balance fitted with a density measurement kit, following Houghton and Wilson (1989).

To obtain the bulk (envelope) clast density, the samples were weighed in air and wrapped in polyethylene film to determine their mass in water (i.e. Archimedes principle). The bulk density was then used to calculate total vesicularity, i.e. the volumetric proportion of all vesicles (connected and isolated) in the pumice clast, using the dense rock equivalent (DRE) density of powdered pumice clasts measured using a Micromeritics AccuPyc II 1345 helium Gas Pycnometer. Since no variation in glass composition and crystallinity across the different tephra horizons was identified (see "Geological background" section), ten clasts were randomly selected and powdered to obtain a representative DRE (2500 kg m^{-3}), which was then used for vesicularity calculations for each clast. Skeletal density of the pumice clasts, including any isolated vesicle space, was also measured using the same instrument. The skeletal and representative powder density measurements were then used to calculate isolated vesicularity, which refers to the ratio between the volume of the vesicles not connected to the surface and the volume of the pumice, including all the vesicles. The difference between the total and isolated vesicularity represents the connected vesicularity. Please refer to supplementary information (SI.1) for the full dataset on the chemical and textural data collected on the ~ 87 ka Baricha pyroclastic deposits.

To ensure representation across the density range, nine juvenile pumice clasts that spanned relatively low-, moderate-, and high-density end members for each stratigraphic horizon were selected for textural analysis. Pumice clasts were prepared as polished thin section by TS Lab and Geoservices, Italy. Additionally, three tube pumice clasts, one from each stratigraphic level, were prepared as polished thin sections cut along directions both orthogonal and parallel to vesicle elongation. For each carbon coated thin section, a set of 15 back-scattered electron (BSE) images were acquired on a JEOL JSM-IT300 scanning electron microscope at the Department of Materials and Chemistry, Vrije Universiteit Brussel (VUB). The images were taken at four different magnifications (30×, 60×, 100×, and 500×) with 320, 580, 985, and 5120 pixels/mm resolution at 15 kV accelerating voltage following the nested image configuration of Shea et al. (2010). The images were processed using ImageJ (Schneider et al. 2012) to remove loose fragments and 3D-like textures, and to manually re-connect visibly broken bubble walls from the thin section polishing process. The images were finally converted into binary 8-bit grey scale images type using the global thresholding algorithm available on ImageJ. The corrected images were then imported into FOAMS software (Shea et al. 2010) to quantify vesicle morphology, vesicle number density (N_V), vesicle volume distributions (VVD), vesicle size distributions (VSD), cumulative volume distributions (CVDs), and cumulative vesicle size distributions (CVSDs). The vesicle volume distributions obtained through FOAMS were normalised by density-derived vesicularity values and a minimum vesicle size of 5 pixels was set as a threshold to be processed by the program.

Results

Granulometry and componentry

The grain size distribution of the ~ 87 ka Baricha deposit of the top, middle, and bottom stratigraphic level of the type section is presented in Fig. 4a. The grain size distributions generally show a high amount of fine to medium lapilli (2–16 mm) with a unimodal distribution, with

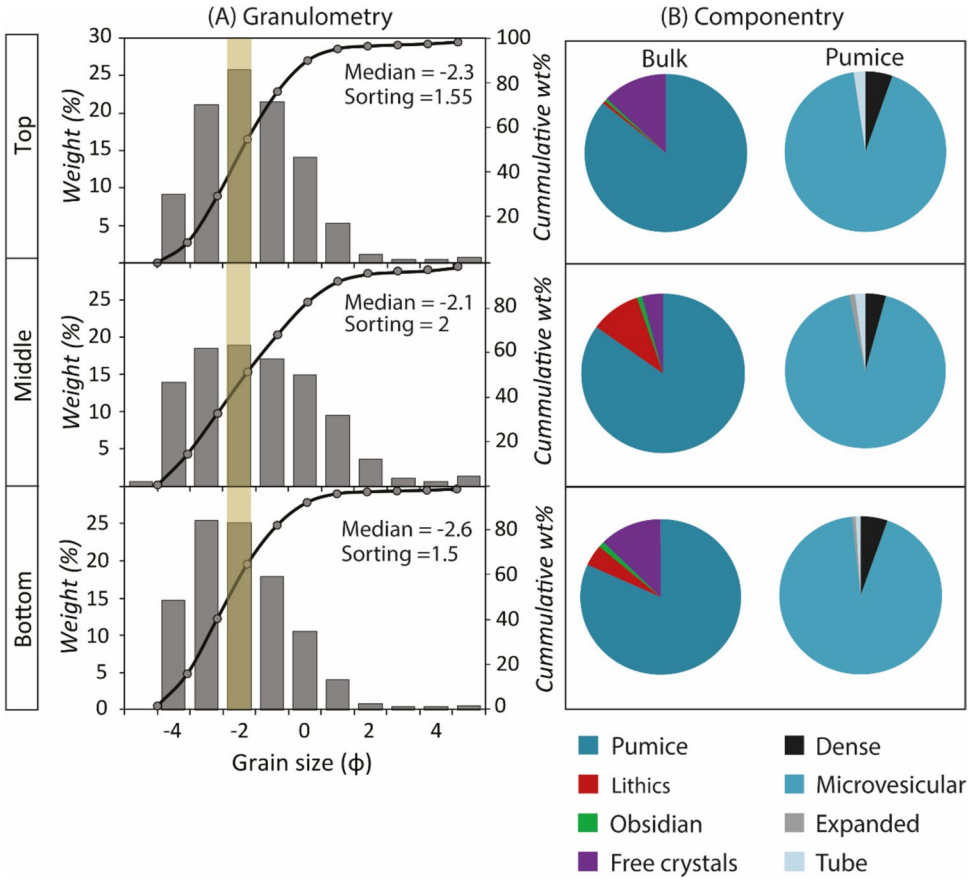

Fig. 4 Granulometry and componentry data plot for the bottom, middle, and top stratigraphic level of ~ 87 ka Baricha deposit. **A** Grain size histogram and cumulative frequency distribution plot for each level. The median size diameter and sorting were calculated based on Inman (1952), and the median size diameter is also indicated by a pale-yellow shaded bar on the histogram plots. Grain size distribution for the pyroclastic density current deposit from the MER205 location is shown in the Appendix (Fig. SI.5). **B** The average componentry data across the grain size fractions of bulk samples and the pumice clasts are presented as pie charts. For componentry charts of each individual grain size fraction, refer to the supplementary information (SI.6)

the mode in the coarser fraction (between -1 and -3ϕ; Fig. 4a). However, the middle stratigraphic level shows an additional small peak in the finer fraction (5ϕ). The median grain diameter is centred at medium lapilli size in all three stratigraphic positions. There is a slight variation of the median from -2ϕ (4 mm) to -2.6ϕ (~ 6 mm) among the different horizons, with the smallest median diameter occurring in the middle horizon. The distribution is skewed towards the coarser grain size, consisting mainly of medium lapilli size and a tail of very fine ash.

The sorting coefficient ranges from 1.5 to 2, and the bottom and top stratigraphic levels (σ_ϕ = ~ 1.5) are relatively better sorted than the middle level of the deposit (σ_ϕ = 2; Fig. 4a). These sorting values of ≤ 2 are consistent with the interpretation of a well-sorted fall deposit (Cas and Wright 1987; Walker 1971). In contrast, the matrix-supported subunit exposed in the middle stratigraphic level to the northwest of the volcano in location MER205 is characterised by a grain size distribution with two modes (-2ϕ and 1ϕ, Fig. SI.5). The median diameter is relatively finer (Md_ϕ = -0.5ϕ) and the sorting coefficient (σ_ϕ = 2.1) is higher than that of the deposit at all stratigraphic levels observed at the reference location, suggesting a PDC deposit, consistent with the field observations (Tadesse et al. 2022).

Componentry analysis of the coarse size fraction (< 1ϕ) shows variable proportions of pumice, lithics, obsidian, and free crystals at different stratigraphic levels (Fig. 4b). Pumice clasts are angular to sub-angular and characterised by a light grey colour. Lithics are composed of slightly altered glassy obsidian, aphanitic lava, or green welded fragments of previous ignimbrite. The obsidian component consists entirely of fresh and crystal-rich chips with a vitreous lustre. The free crystal fraction includes alkali feldspar, quartz, aenigmatite, clinopyroxene, amphibole, and Fe-Ti oxides. The deposit is dominated by pumice clasts (≥ 25%) in all observed grain size classes, with a lower proportion in the finer fractions (1ϕ; Fig. SI.6). In contrast, lithics, obsidian, and free crystals are abundant only in the finer fraction (≥ -1ϕ; Fig. SI.6). The average componentry indicates consistent pumice (81–86%) and obsidian (≤ 1%) proportions at different stratigraphic levels. On the other hand, the lithics and free crystals show marked variations. Lithic content is higher in the middle stratigraphic level (17%) than in the bottom (6%) and top horizons (~ 1%), and the proportion of free crystals is consistently 13% at the bottom and top, and higher in the middle stratigraphic level (17%; Fig. 4b).

Based on macroscopic observations of textural variability such as colour, external morphology, and vesicularity, the pumice component is further categorised into four types:

dense, microvesicular, expanded, and tube pumice, as described by Polacci et al. (2003) and Tadesse et al. (2022). Microvesicular pumice is the dominant type, accounting for more than 77% of the deposit in all grain size classes, with insignificant and non-systematic variations in the other pumice types observed in different grain size classes (Figs. 4b and SI.6). Moreover, the average of all the considered grain size classes similarly indicates an abundance of microvesicuar pumice (92–93%) and an almost consistent proportion of it throughout the stratigraphy. A low proportion of dense pumice is also present (~5%) and shows a minor decrease in the middle stratigraphic level (~4%). Expanded and tube pumice classes represent only a small proportion (≤2%) and show slight variations along the stratigraphy (Fig. 4b).

Density and vesicularity of pumice

The bulk density of the pumice clasts exhibits a wide range from 90 to 1,000 kg m^{-3}, and the distribution is unimodal with the highest frequency at moderate density values of 400–700 kg m^{-3} (Fig. 5a). Microvesicular pumice is the primary constituent of the moderate-density clasts, while the low-density clasts (< 400 kg m^{-3}) are mostly expanded and long-stretched tube pumice. On the other hand, the high-density clasts (> 700 kg m^{-3}) are almost entirely composed of the dense pumice identified in the componentry analyses. The low-density tail progressively increases up the stratigraphic sequence, while the high-density tail is only significant in the bottom and middle stratigraphic levels of the deposits (Fig. 5a).

The range of bulk densities of the pumice clasts predominantly corresponds to a range of total vesicularity values of 60–90%, with only few clasts ($n=5$) showing a total vesicularity of up to 96% (Fig. 5b). These vesicularity values fall in the highly to extremely vesicular range defined by Houghton and Wilson (1989). The average total vesicularity of the pumice gradually decreases from low-density (90 ± 2%) to high-density clasts (67 ± 4%) (Fig. 5b). The total vesicularity is predominantly connected vesicularity (~65–90%) with only a small proportion of isolated vesicularity (≤6%; Fig. 5b). The average connected vesicularity is higher in low-density clasts (90 ± 3%) than in

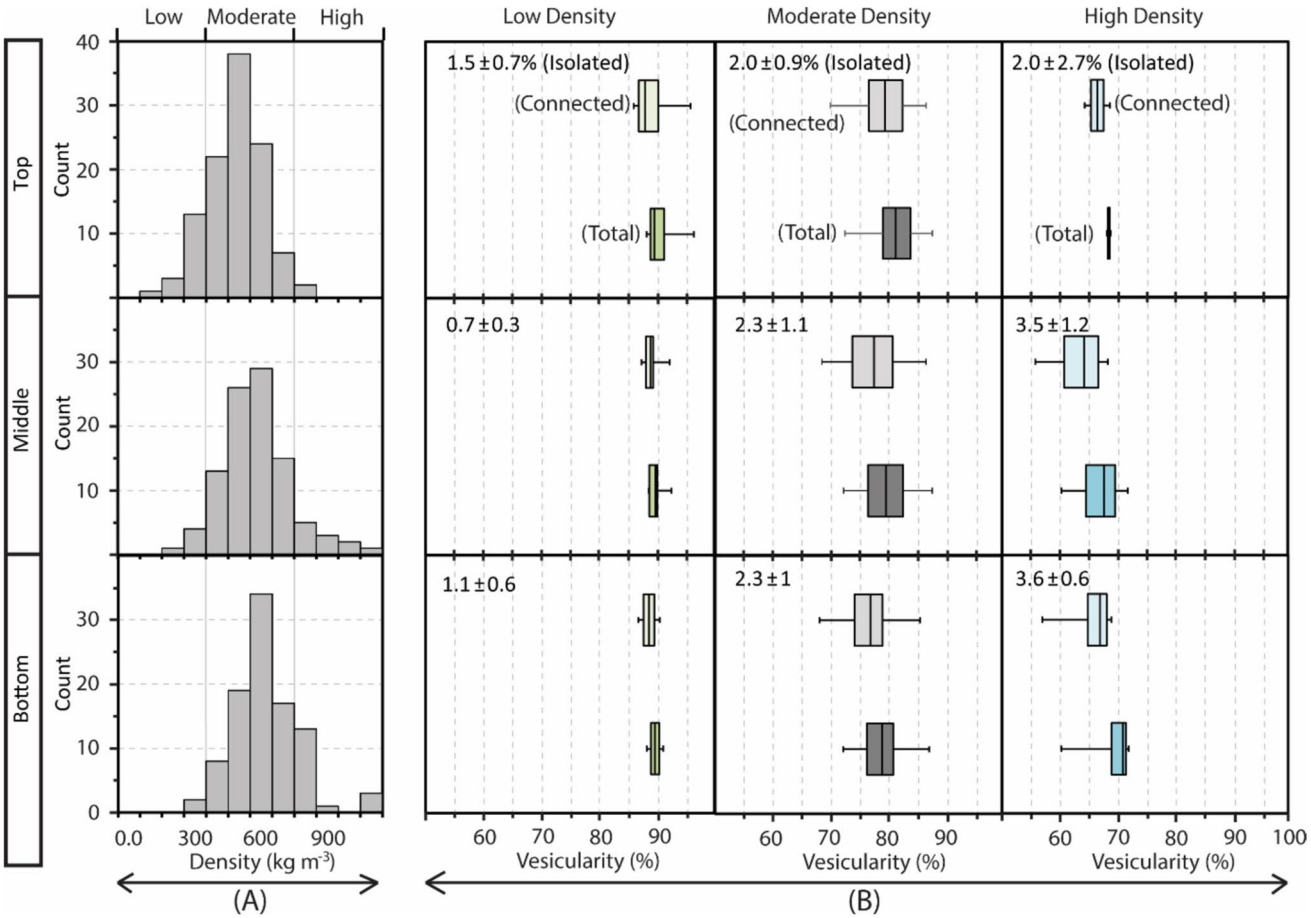

Fig. 5 Pumice density (**A**) and vesicularity (**B**) distribution plots for the bottom, middle, and top stratigraphic level of the ~ 87 ka Baricha deposit measured on > 100 clasts for each level. The total and connected vesicularity is plotted separately on the box plots, while the average and standard deviation of the isolated vesicularity are indicated on each panel. The low-, moderate-, and high-density category for the vesicularity box plots is based on the pumice clast density distribution of (**A**)

high-density pumice (64–80 ± 4%). Furthermore, the connected vesicularity for each type of pumice shows a progressive slight increase with stratigraphy, while isolated vesicularity remains constant throughout the stratigraphy (Fig. 5b).

Microscopic textures of pumice

Qualitative description

The analysed pumice are characterised by an extended range of textures (Fig. 6). Vesicles cover a broad size range, from 0.001 to 2.4 mm. Coalescence of vesicles is more apparent in low-density clasts, in which vesicles are larger, covering the higher size range (Fig. 6). Coalescence is indicated by vesicle wall flattening, thinning, wrinkling, failure, and retraction at boundaries between adjacent vesicles that are coalescing, primarily on larger vesicles (Klug and Cashman 1996). Smaller-size vesicles (< 0.01 mm) are typically more spherical and do not exhibit signs of coalescence (Fig. 6).

Within each stratigraphic level, vesicles gradually become smaller and show less coalescence in the high-density

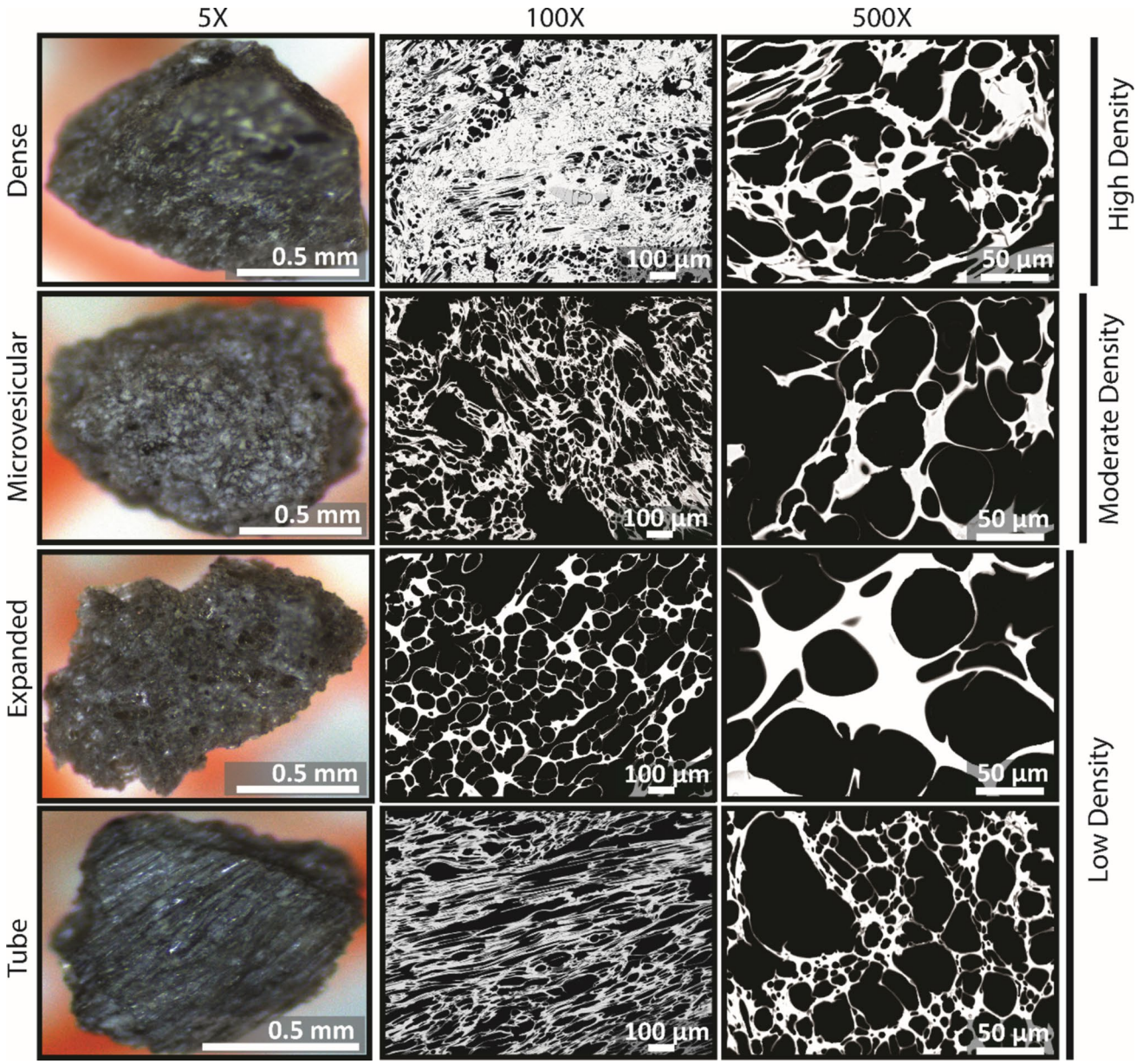

Fig. 6 Selected images of various types of pumice clasts taken by stereo-microscope and SEM at different magnifications (5×, 100×, and 500×). The pumice clasts are representative of the different clast types (i.e. tube, expanded, microvesicular, and dense). The binary images of the tube pumice are from thin sections cut parallel (100×) and perpendicular (500×) to the dominant vesicle elongation

pumice. In these high-density pumice, small, rounded vesicles make up a densely packed texture. In a few cases, there are localised distributions of small-sized, stretched vesicles in high-density pumice, which may have resulted from the collapse of larger vesicles (Fig. 6). Vesicle walls are predominantly < 10 µm thick in low-density pumice, while in high-density clasts, they show a wide thickness range (i.e. < 10–80 µm; Fig. 6). In addition to coalescence, extensive micro-fractures are visible in most pumice, which can increase permeability by connecting adjacent vesicles.

Vesicle morphology

The pumice analysed in this study exhibit a wide range of vesicle shapes, ranging from spherical to complexly coalesced (Fig. 7). The vesicle morphologies in all density ranges and stratigraphic positions are predominantly regularly shaped (rg = > 0.9), where the regularity parameter (rg) is defined as the ratio of vesicle area to the corresponding best-fit ellipse area (Shea et al. 2010). Vesicle shape can also be characterised by elongation (ε), which measures the degree of deformation of the vesicles and is calculated as (a—b) / (a + b), where a and b are the best-fit ellipse semi-long and semi-short axes, respectively (Shea et al. 2010). Elongation shows a unimodal distribution for all analysed clasts, with a main mode between 0.3 and 0.7. Similarly, the aspect ratio (AR = b/a) is > 0.5 for the majority of the vesicles, meaning they can be classified as moderately to slightly elongated vesicles according to Blott and Pye (2008). However, the low-density pumice collected from the top stratigraphic level contains a significant proportion of stretched vesicles with an elongation value of < 0.5 (Fig. 7). The sections of tube pumice (moderate- and low-density) cut parallel and perpendicular to the vesicle elongation show high vesicle elongation in one direction only (parallel) and a high abundance of sub-spherical to ellipsoidal vesicles in the perpendicular orientation (Fig. 6).

Vesicle volume and size distributions

The distributions of vesicle volumes can be observed in plots of volumetric percentage versus equivalent vesicle diameter (L in mm; Fig. SI.7). Across all density ranges, the analysed pumice exhibits a wide range of vesicle sizes (ranging from 0.001 to 2.4 mm), although the distribution tends to shift towards smaller sizes in high-density pumice. The distribution of vesicle sizes is polymodal for all analysed pumice clasts (Fig. SI.7). Whereas the modes are distinct for the low- and moderate-density pumice, they are less prominent for high-density clasts. The low-density

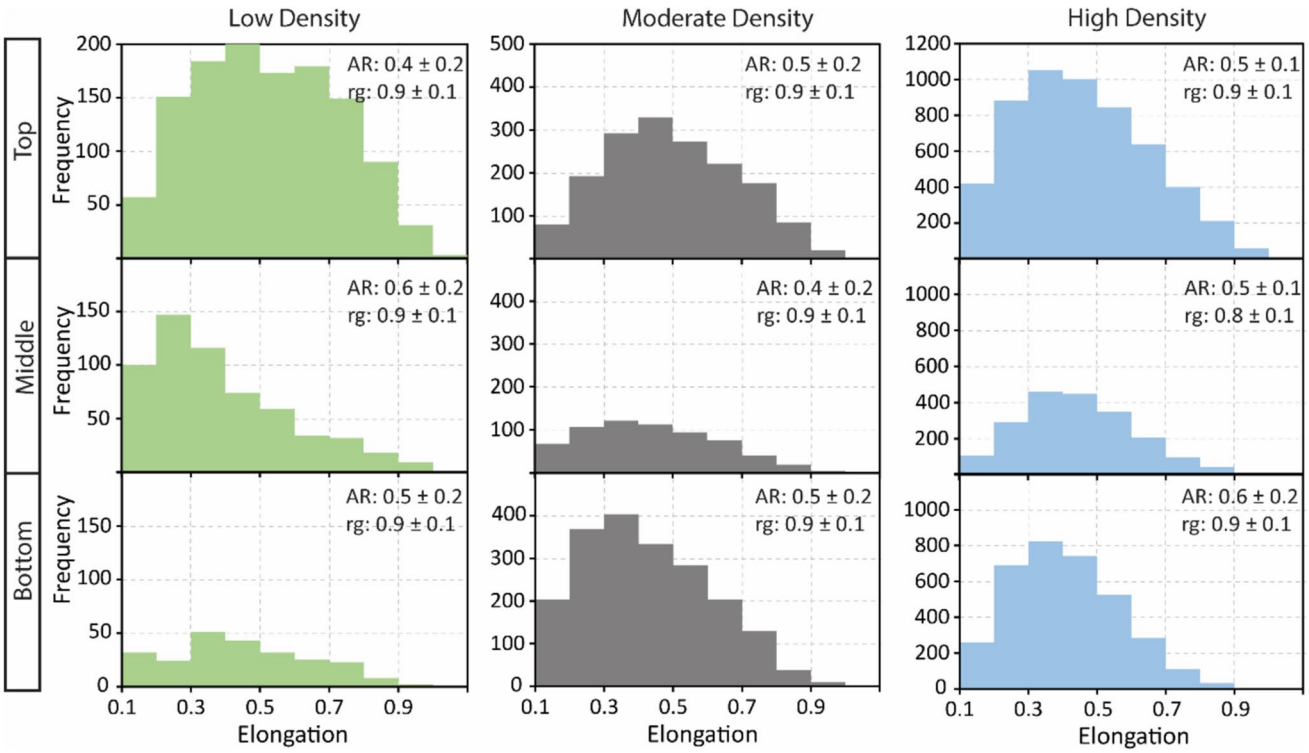

Fig. 7 Vesicle elongation histogram plots of low-, moderate-, and high-density pumice collected from bottom, middle, and top stratigraphic levels of ~ 87 ka Baricha deposits. A total of 15 pumice clasts was prepared and analysed, while only the 9 representative clasts are presented in this figure. The aspect ratio (AR) and regularity (rg) mean and standard deviation values are indicated on each plot

pumice clasts, in general, lack smaller vesicles (< 10 μm), except those from the top stratigraphic level which contain a few percent of small vesicles (Fig. SI.7).

The trends of cumulative volume distributions are distinct for low-density and high-density pumice, as shown in Fig. 8. The curves are sigmoidal in shape and have several breaks in slope. The Log ($N_V > L$) against the equivalent diameter plots show a break in slope at L ~ 30 μm, which is highlighted by the vertical lines in Fig. 8. For vesicle diameters larger than 30 μm, the distribution follows a linear trend with an average slope of -3.2 (Fig. 8). However, the trend for smaller vesicles (< 30 μm) deviates and shows a gentler trend with an average slope of -1.3 (Fig. 8).

Vesicle number densities

The vesicle number densities per unit area of image (N_A) for all pumice examined using 2D image analysis range from $0.37*10^3$ to $3.74*10^3$ mm^{-2}. Vesicle number per unit volume ranges from $0.07*10^7$ to $1.59*10^7$ mm^{-3}, calculated using stereo conversion with the assumption of spherical vesicle geometry as per Sahagian and Proussevitch (1998). The vesicle number density is corrected for vesicularity and crystallinity (N_V^M), and it ranges between $0.05*10^7$ to $1.53*10^7$ mm^{-3}. However, tube pumice have higher apparent N_V^M values (> $1*10^8$ mm^{-3}) due to extreme vesicle elongation that invalidates the spherical vesicle assumption. Therefore, only vesicle number density per unit volume results are reported for pumice clasts with less elongated vesicles, with a range of $0.05–0.8*10^7$ mm^{-3} for low-density samples to $0.44–1.53*10^7$ mm^{-3} for moderate- and high-density samples. The vesicle number density of low-density pumice progressively increases from the bottom ($0.05*10^7$ mm^{-3}) to the top ($0.8*10^7$ mm^{-3}) stratigraphic level, while it remains consistent for high-density pumice ($1.1*10^7$ mm^{-3}). The moderate-density clasts generally show a lower vesicle number density at the middle stratigraphic level ($0.44*10^7$ mm^{-3}) and higher values at the top stratigraphic position ($1.53*10^7$ mm^{-3}; Table 1).

Decompression rate

Vesicle number densities provide an opportunity to estimate magma decompression rates using Toramaru´s equation (Toramaru 2006):

$$Nv = 34C_o\left(\frac{16\pi\sigma^3}{3kTP_o^2}\right)^{-2}\left(\frac{V_M P_o}{KT}\right)^{-\frac{1}{4}}\left(\frac{KTC_o DP_o^2}{4\sigma^2\left|\frac{dP}{dt}\right|}\right)^{-3/2}$$

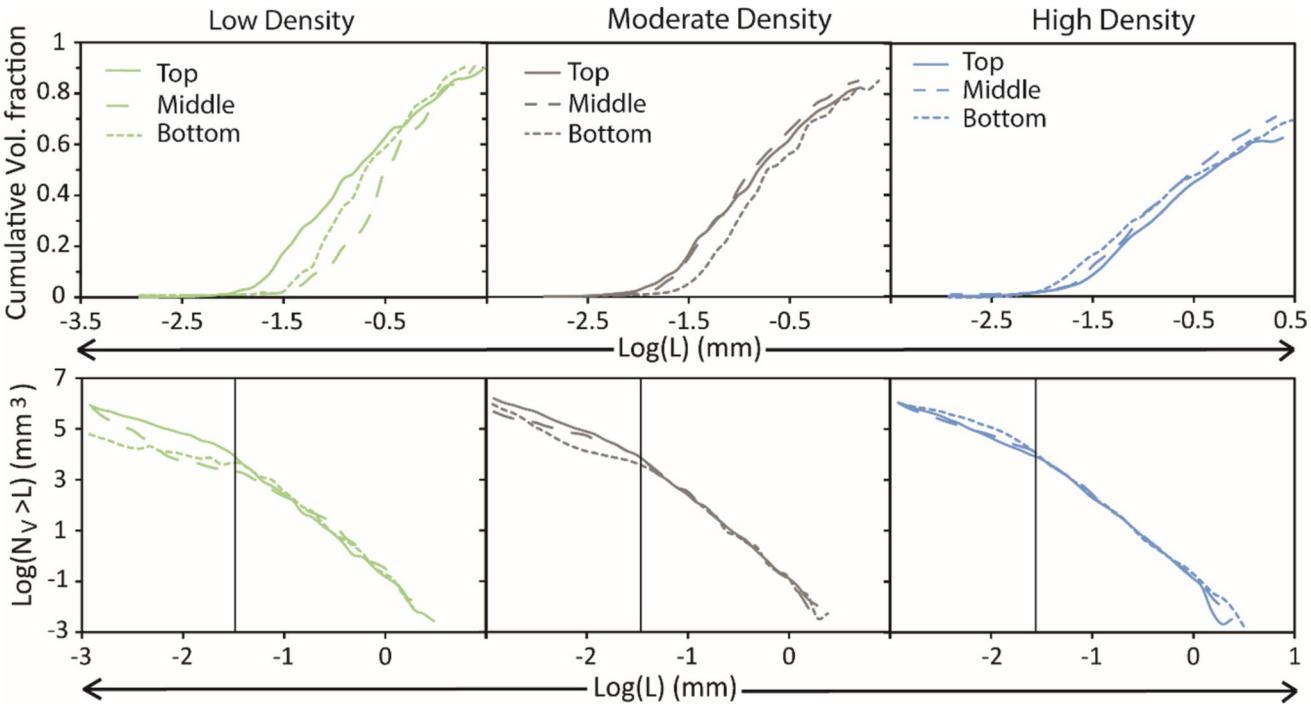

Fig. 8 Cumulative vesicle size distribution of low-, moderate-, and high-density pumice collected from bottom, middle, and top stratigraphic levels of the ~ 87 ka Baricha deposit. L is the equivalent vesicle diameter in mm. The multiple bulges on the cumulative volume fraction against Log (L) plots observed for low- and moderate-density clasts are less pronounced for the high-density pumice. The Log ($N_V > L$) against Log (L) plots show a pronounced break in slope for all clasts, indicated by the solid vertical lines

Table 1 Vesicle number density, decompression rate and vesicle morphology (AR: Aspect ratio, Ɛ: elongation, rg: regularity) of the moderate-density pumice clasts for the lower, middle, and top stratigraphic levels of the ~ 87 ka Baricha eruption deposit. The decompression rate is calculated for both homogeneous (dP/dt_{homo}) and heterogeneous (dP/dt_{hetro}) nucleation conditions using the empirical relationship from Toramaru (2006)

Stratigraphic position	Clast type	N_A (mm^{-2}) * 10^3	N_V (mm^{-3}) * 10^7	N_V^M (mm^{-3}) * 10^7	dP/dt_{homo} (Mpa/s)	dP/dt_{hetro} (Mpa/s)	AR	Ɛ	rg
Bottom (2A)	Dense	2.65	1.12	1.09	4.4	0.51	0.50	0.36	0.87
	Expanded	2.52	0.86	0.80	3.6	0.42	0.44	0.42	0.86
	Microvesicular	3.74	1.59	1.53	5.6	0.64	0.46	0.40	0.88
Middle (2B)	Dense	2.65	1.14	1.09	4.5	0.52	0.51	0.35	0.84
	Expanded	0.90	0.69	0.68	3.2	0.38	0.59	0.29	0.87
	Microvesicular	1.71	0.48	0.44	2.4	0.28	0.52	0.34	0.90
Top (2C)	Dense	4.04	1.14	1.05	4.3	0.50	0.55	0.31	0.87
	Expanded	0.37	0.07	0.05	0.6	0.07	0.51	0.35	0.89
	Microvesicular	1.51	0.92	0.90	4.0	0.46	0.54	0.33	0.89

where N_V is measured vesicle number density (mm^{-3}); C_o the initial water concentration at saturation pressure (wt%); dP/dt the decompression rate (MPa/s); k the Boltzmann constant ($=1.38\times10^{-2}$ J/K); V_M the volume of water molecules in the melt ($=3\times10^{-29}$ m^3; Toramaru 1989); P_o the saturation pressure (MPa); T the temperature (K); σ the surface tension (N/m) and D the water diffusivity (m^2/s). Following Shea et al. (2011), only the number densities of the smallest vesicle population (0.001–0.01 mm) are considered to capture the decompression rates that correspond to the final stages of the ascent rate prior to fragmentation. The rhyolite magma feeding the eruption is characterised by 75 wt% SiO_2, 5 wt% H_2O, 1003 K temperature and 100 MPa storage pressure (Tadesse et al. 2023b). The saturation pressure is assumed to be equivalent to the storage pressure to calculate the decompression rate. As the pumice are microlite-free, we applied Eq. 13 of Shea (2017) to calculate the surface tension (=0.072 N/m). However, nanolites (< 1000 µm crystals) have been suggested to favour heterogeneous bubble nucleation (e.g. Shea 2017; Cáceres et al. 2020; McCartney et al. 2024). To account for potential errors arising from the undetected presence of nanolites, we applied surface tension values reported in previous works for heterogeneous nucleation on Fe-Ti oxides (i.e. 0.017–0.03 N/m; Shea 2017 reference therein). The empirical relation (Eq. 6) of Toramaru (2006) is applied to calculate the water diffusivity. To test the validity of the decompression rate calculation, we accounted for realistic analytical errors in SiO_2 and H_2O contents by applying a variation of ± 1–2 wt% on each. Using this wider range for both SiO_2 and H_2O in the calculation resulted in changes of less than ± 2 MPa/s in the decompression rate.

The decompression rate estimated using the Toramaru (2006) equation under homogeneous nucleation conditions falls within the range of 0.6–5.6 MPa/s, while for heterogeneous nucleation it averages between 0.07 and 0.64 MPa/s. The decompression rate calculated for both nucleation conditions show lower estimates for the low-density pumice (dP/dt_{homo}: 0.6–3.6 MPa/s; dP/dt_{hetro}: 0.07–0.42 MPa/s) than for the moderate- to high-density pumice (dP/dt_{homo}: 2.4–5.6 MPa/s; dP/dt_{hetro}: 0.28–0.64 MPa/s). Among the different density classes, the low- and high-density pumice show a progressive increase in decompression rate from bottom to top stratigraphic levels, while the moderate-density pumice display higher decompression rates at the bottom (dP/dt_{homo}: 4 MPa/s; dP/dt_{hetro}: 0.46) and top (dP/dt_{homo}: 5.6 MPa/s; dP/dt_{hetro}: 0.64) levels compared to the middle level (i.e. dP/dt_{homo}: 2.4 MPa/s; dP/dt_{hetro}: 0.28). These results suggest that the decompression rate varies depending on the pumice density and stratigraphic position, and that the decompression rate was relatively higher during the beginning and final stages of the eruption (Table 1).

Discussion

The ~ 87 ka Baricha deposit presents a unique opportunity to study variations in the dynamics of peralkaline rhyolite magmas within a single eruption. The deposit exhibits angular clast shapes, consistent thickness at the outcrop-scale (Tadesse et al. 2022), and well-sorted grain size distributions, all indicative of a pyroclastic fall emplacement mechanism for the three different horizons of the deposits at the reference location. Conversely, the middle horizon exposed to the NW of the volcano (e.g. MER205, MER301) is characterised by poorly sorted and matrix-supported PDC deposits. There is no evidence for significant time breaks (e.g. alteration, palaeosols) between the different horizons, suggesting that they represent three major phases of the same eruption. We will refer to these as phase 1 (bottom), 2 (middle) and 3 (top).

The massive and relatively well-sorted horizons in the bottom and top stratigraphic level (phases 1 and

3) are interpreted as products of a sustained eruption period characterised by a buoyant eruption column. In contrast, the middle stratigraphic level (i.e. phase 2) is characterised by cm-to-dm scale parallel bedded fall and associated PDC deposits, indicating an unsteady column and pulsatory behaviour (Cioni et al. 2015; Houghton and Carey 2015). Overall, the ~ 87 ka Baricha tephra deposit suggests a switch in eruption behaviour from a sustained phase to unsteady behaviour, followed by another sustained plume phase.

Bubble evolution

The total vesicularity of pumice clasts from the ~ 87 ka Baricha eruption is consistently high (≥ 60%). This aligns with the typical characteristics of products from silicic explosive eruptions (Gardner et al. 1996; Klug and Cashman 1996; Polacci et al. 2001; Klug et al. 2002; Gurioli et al. 2005; Houghton et al. 2010). The presence of a few highly expanded pumice clasts with > 90% total vesicularity may suggest a minor role of post-fragmentation effects in the vesiculation history of the clasts (Cashman and Scheu 2015). To eliminate these minor post-fragmentation expansion effects, bubble walls on the BSE images were reconnected for the 2D textural analyses, described in "Methods" section. Moreover, overall pumice textures show high vesicle number densities, ranging in the order of 10^6 to 10^7 mm^{-3}, values similar to those observed in pumice clasts from other Plinian-style eruptions (Klug and Cashman 1996; Klug et al. 2002; Gurioli et al 2005; Houghton et al. 2010; Rust and Cashman 2011).

The majority of total vesicularity is represented by connected vesicularity, a good indicator of bubble interconnectivity and thus permeability (Gardner et al. 1996; Klug and Cashman 1996; Klug et al. 2002; Shea et al. 2012; Alfano et al. 2012). The corresponding connectivity (the ratio of connected to total vesicularity; e.g. Colombier et al. 2017a) ranges between 0.91 and 1, emphasizing the significance of connected vesicles in forming a permeable network. The connected vesicularity and thus vesicle interconnectivity progressively increases from high- to low-density pumice (Fig. 5). The vesicle number densities recorded in the low-density pumice are very low (0.07–0.86*10^7 mm^{-3}) compared to the other types (0.48–1.59*10^7 mm^{-3}), whereas the variation in vesicle number density along the stratigraphy for moderate- and high-density pumice is non-systematic and does not show any relation with the vesicularity data. The combination of the vesicularity and vesicle number density suggests a progressive increase in permeability favouring gas escape in the final phase of the eruption. Such an increase in permeability within the foam facilitates volatile loss, which eventually leads to waning of the explosive eruption (Klug and Cashman 1996; Klug et al. 2002; Castro et al. 2012).

The cumulative vesicle size plots reveal a change in slope around ~ 30 µm vesicle size in all types of pumice, characterised by two populations of vesicles following power-law trends (Fig. 8). The smaller vesicle sizes (< 30 µm) show a power-law relationship with an average exponent (d) of 1.3, implying non-equilibrium, continuous, and/or accelerating nucleation and growth (e.g. Blower et al. 2003; Alfano et al. 2012; Colombier et al. 2017b; Hughes et al. 2017). The moderate-to-large size vesicles (> 30 µm) are also governed by a power-law relationship, but with a higher d value (= 3.2) attributed to bubble coalescence overprinting nucleation (Gaonac'h et al. 1996; Klug et al. 2002; Giachetti et al. 2010; Alfano et al. 2012; Hughes et al. 2017). The latter case is also seen qualitatively in the BSE images, where the larger-size individual bubbles begin to interact and often form larger irregular-shaped bubbles (Fig. 6). Similar changes in slope of the power-law trend are reported for pumice from other eruptions (e.g. Klug et al. 2002; Houghton et al. 2010; Colombier et al. 2017b), possibly caused by bubble coalescence overprinting continuous nucleation (GaGaonac'h et al. 1996: Blower et al. 2003). The 1.3 exponent value is comparable to that reported for vesicles of similar size in different eruptions (e.g. Blower et al. 2003; Alfano et al. 2012; Hughes et al. 2017), suggesting that the development of small bubbles reflects the final stage of decompression shortly before fragmentation. The microlite-free nature of the pumice samples likely indicates that the final stage of the decompression was very rapid, and prevented nucleation and growth of microlites.

Eruption style and parameters

Previous studies have suggested a positive correlation between bubble number density and mass discharge rate (Houghton et al. 2010; Rust and Cashman 2011; Alfano et al. 2012; Shea 2017). However, this relationship seems to be stronger for near-equilibrium vesiculation conditions than for disequilibrium ones (Rust and Cashman 2011; Alfano et al. 2012; Shea 2017). In the context of Plinian-style eruptions, the calculated mass discharge rates may have a significant uncertainty (Rust and Cashman 2011; Alfano et al. 2012; Shea 2017). Based on Shea´s (2017) relationship between decompression and magma discharge rate, it was estimated that the mass discharge rate of the ~ 87 ka Baricha eruption during its three phases was on the order of 10^6–10^7 kg/s, considering the measured bulk density, and assuming a constant vent radius of 10 m (Campagnola et al. 2016; Hughes et al. 2017). The equivalent maximum plume height (H_T) was estimated to range between 10 and 30 km, based on the equation from Carey and Bursik (2015): $H_T = 1.67Q^{0.259}$. The mass discharge rate (m) was converted to volumetric discharge rate (Q) by applying a dense rock equivalent of 2500 kg/

m^3 measured in this study. However, it should be noted that assuming a constant conduit radius throughout different eruption phases, given the variations in lithic proportions, oversimplifies the model and may result in a relative underestimation of the mass discharge rate and plume height for the second and third eruption phases.

To calculate the plume height, the maximum lithic size is utilised, and the particle sedimentation model of Rossi et al. (2019) is applied. This model, modifying the methodology proposed by Carey and Sparks (1986), considers the effects of wind on the eruptive column. However, since the maximum lithic size (ML) value is available only from one location, isopleth contours are extrapolated concentrically to the deposit isopach contours (Fig. 2). Employing a clast density of 2500 kg/m^3 and an ML of 1.6 cm gives a plume height estimate of ~ 17 km. This value falls in the wider calculated estimate from vesicle number density, demonstrating uncertainty in either or both methods. Regardless, the plume height (10–30 km) and the mass discharge rate calculated from either method (i.e. vesicle number density and maximum clast size) collectively suggest a Plinian-style (subplinian to Plinian) eruption (Bonadonna and Costa 2013).

Eruptive column behaviour and dynamics

Fluctuations in eruption behaviour are primarily attributed to processes within magma reservoirs and their conduits during magma ascent (Cassidy et al. 2018). The ~ 87 ka Baricha eruption serves as an excellent case to examine the factors governing the transition of column behaviour from sustained to unsteady behaviour. Similar to the vesicle number density, the decompression rate for the ~ 87 ka Baricha pumice displays significant variation among the different eruption phases and pumice types. The decompression rate, in general, varies between 0.07 and 5.6 MPa/s, which is lower relative to most Plinian-style eruptions for which data are available, e.g. 2008 Chaitén (8.1 ± 2.9 MPa/s) and 1875 Askja (38.2 ± 12.3 MPa/s) (Shea 2017, and references therein). The low-density pumice (i.e. dp/dt_{homo}: 0.6–3.6 MPa/s; dp/dt_{hetro}: 0.07–0.42 MPa/s) yield the lowest decompression rates relative to microvesicular and dense pumice (i.e. dp/dt_{homo}: 2.4–5.6 MPa/s; dp/dt_{hetro}: 0.28–0.64 MPa/s). The expanded and tube pumice clasts are mainly characterised by an elongated vesicle morphology and interconnected vesicles that mainly result from high strain rate deformation during fragmented magma flow close to the conduit walls (e.g. Klug and Cashman 1996; Marti et al. 1999; Polacci et al. 2003; Dingwell et al. 2016). Since the low- and high-density pumice are very rare (< 10%), the moderate-density pumice and related parameters represent the bulk of the magma. The decompression rates for the moderate-density pumice exhibit minor fluctuations across the three major eruption phases; 4 MPa/s or 0.46 MPa/s (phase 1), 2.4 MPa/s or 0.28 MPa/s (phase 2), to 5.6 MPa/s or 0.64 MPa/s (phase 3), under homogeneous or heterogeneous nucleation conditions, respectively. These minor changes align with the shifts in eruption dynamics and suggest varying conduit conditions during the different eruption phases, including periods of relatively slow ascent in the shallow conduit during phase 2.

The middle stratigraphic level of the eruption deposit, characterised by the highest lithic content, is likely associated with vent widening during the pulsatory eruption phase. This increase in vent radius could lead to variations in exit conditions (Carey et al. 2009) and/or an increase in the lateral extent of the eruptive column base, reducing efficiency of air entrainment and resulting in an unsteady column (e.g. Wilson et al. 1980). The incorporation of large amounts of lithics into the eruptive mixture could also increase the bulk plume density, further promoting unsteady behaviour and column collapse (e.g. Shea et al. 2011; Pardo et al. 2014). However, the high-density juvenile clasts remain almost constant throughout the eruption, suggesting a minor or no role of magma densification in the partial collapse of the eruption column. Consequently, a combination of higher plume density, an increasing vent radius, and a lower decompression rate due to a decrease in volatile pressure in the conduit is likely responsible for the transition in eruption dynamics from steady (phase 1) to unsteady (phase 2) plume behaviour. Conversely, an increase in decompression rate and a well-connected conduit system during the last eruption phase likely generated a sustained plume phase.

Because there is no significant variability in glass composition among the first two eruption phases, the chemical composition of the magma may not have a first-order influence on the observed variation in the eruption dynamics. The glass and feldspar compositions of the volcanic products from the last phase remain similar to those of the first two eruption phases (Figs. 3, SI.1, and SI.2; Tadesse et al. 2023b). However, the amphiboles in a few crystals show an increasing Mg content between phase 1 and phase 3, interpreted as crystals progressively sourced from deeper storage levels (Tadesse et al. 2023b). Aenigmatite crystals in the third eruption phase are richer in Mg, Ca, and Al compared to the first phase (Fig. SI.4). This enrichment is interpreted as the result of injecting fresh and more mafic magma into the shallow peralkaline magma plumbing system (Sparks et al. 1977; Ruprecht and Bachmann 2010; Degruyter et al. 2016). The addition of hot and volatile-rich magma may have caused the ascending magma to regain higher decompression rates and increased mass discharge rates during the last eruption phase.

The efficiency of degassing is largely governed by magma composition and rheology (Di Genova et al. 2013). The rhyolite magma feeding the ~ 87 ka Baricha eruption

is characterised by an alkaline-rich composition (mol% $(K_2O + Na_2O)/Al_2O_3$: 1.4–1.8; Tadesse et al. 2023b). Melt inclusion analyses of peralkaline rhyolite products from other volcanoes in the MER region show volatile-rich melts with < 2–8 wt% H_2O (av. 5 wt%), ~ 4000 ppm Cl, and 7000 ppm F (Iddon et al. 2019). The viscosity of the peralkaline rhyolite magma from the ~ 87 ka Baricha eruption ranges from $10^{7.5}$ to 10^9 Pa.s under hydrous conditions (5 wt% H_2O) at a storage temperature of 1003 K, according to the mathematical relationship proposed by Di Genova et al. (2013). This viscosity range aligns with that calculated for pumice achneliths from Aluto volcano in the MER ($10^{7.7}$ Pa.s; 1023 K, 1 wt% H_2O; Clarke et al. 2019) and pumice clasts from the Cuddia di Mida eruption at Pantelleria (10^4–$10^{7.5}$ Pa.s; 1075 K, 0–1 wt% H_2O; Hughes et al. 2017). Brittle magma fragmentation occurs when a strain rate dependent viscosity exceeds 10^8–10^9 Pa.s (Di Genova et al. 2013, and references therein). The viscosities exhibited by the ~ 87 ka Baricha, Aluto, and Cuddia di Mida peralkaline rhyolite magmas are within or below this critical range, suggesting that additional factors, such as degassing and crystal enrichment, take place to increase viscosity and lead to a brittle fragmentation mechanism to drive explosive eruption (Hughes et al. 2017).

The ~ 87 ka Baricha eruption comprises three primary Plinian-style phases, as illustrated in Fig. 9. During the first phase, magma with high volatile content rapidly ascended through the conduit, generating a sustained convective plume that deposited massive tephra fall at the bottom stratigraphic level. In the second phase, the plume became unsteady and collapsed due to lower decompression rates and mass discharge rates compared to the first phase. Lithic-rich bedded tephra fall and associated PDC deposits record the conduit-widening processes that occurred during this phase. The third phase displays renewed sustained plume behaviour, resulting from gas-rich magma ascending at a higher ascent rate after (cryptic) addition of more mafic magma. The injection of this more mafic magma may have occurred before the initiation of the eruption, creating a stratified reservoir and stayed unmixed for a while (e.g. Shamloo and Grunder 2023). As the eruption progressed and the volatiles in the older resident magma were depleted, the more mafic magma began to mix, increasing volatile content and causing magma overpressurization, which renewed the sustained eruptive column. The sustained column from this third phase resulted in a massive tephra fall deposit. The higher proportion of highly inflated pumice and increased vesicularity indicate a prolonged bubble development that established permeable networks to degas volatiles, and which eventually led to eruption waning.

The integration of the conceptual magma flow and eruption dynamics model presented in this study sheds new light on the behaviour of moderate to large peralkaline rhyolite eruptions. Deposits resulting from these eruptions are typically thick at proximal sites and quickly thin out within tens of kilometres from the source vent. These field characteristics are similar to those observed for other peralkaline rhyolite eruptions in the MER (e.g. Aluto: Fontijn et al. 2018: Clarke et al. 2019; Corbetti: Colby et al. 2022) and Pantelleria, Italy (e.g. Cuddia di Mida: Hughes et al. 2017). Our detailed evaluation of the tephra deposits, consistent with other studies on pumice-cone-forming eruptions (Clarke et al. 2019), suggest that highly unsteady subplinian to Plinian eruption columns were responsible to generate deposits with limited lateral extent.

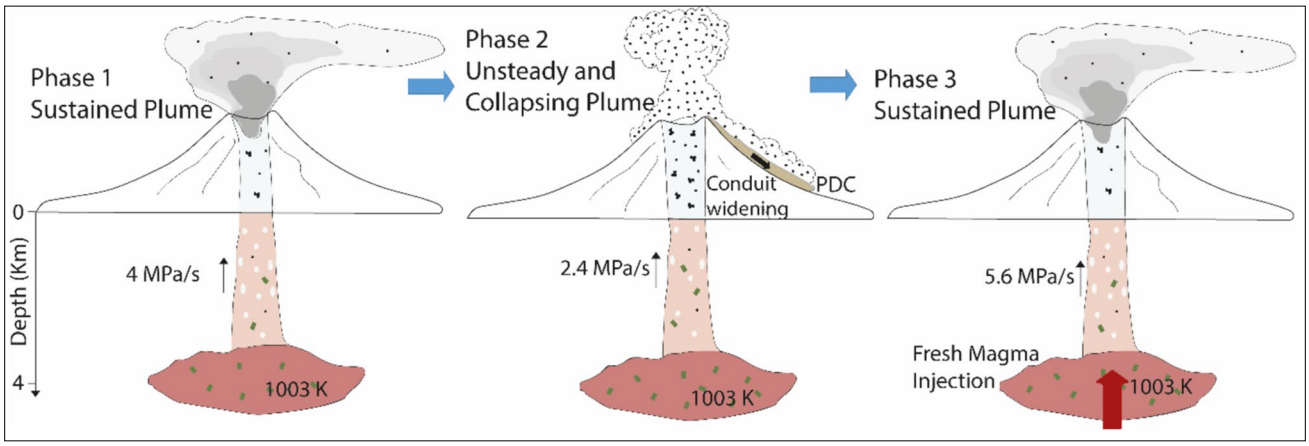

Fig. 9 Schematic diagram illustrating the history of magma dynamics and plume behaviour during the ~ 87 ka Baricha eruption. Decompression rate (dP/dt) is calculated after Toramaru (2006). Magma composition and pre-eruptive conditions (depth and temperature) are after Tadesse et al. (2023b). Note that the pre-eruptive storage temperature is based on feldspar-related thermometers, and indicate consistent values throughout the eruption

Conclusion

The study of the ~ 87 ka Baricha explosive eruption products has provided new valuable insights into the dynamics of peralkaline magma during its different eruptive phases. The eruption deposits exhibit three distinct horizons, each associated with three different eruptive phases. The massive and relatively well sorted tephra fall horizons in the bottom and top stratigraphic levels are deposited from sustained plumes. The middle stratigraphic level displays internally bedded lithic-rich tephra fall, suggesting an unsteady plume developed during a vent-widening phase. The analysis of the pumice from all levels of the deposit reveals a bulk density ranging from 400 to 700 kg m^{-3}, > 60% total vesicularity, and an absence of microlites. The vesicle number density, derived from textural analysis, falls in the range of $0.07*10^7$ to $1.6*10^7$ mm^{-3}, comparable to other Plinian-style eruptions. Similarly, decompression rates of the ascending magma vary from 0.07 to 5.6 MPa/s, with a significant drop observed during the second eruption phase. The polymodal vesicle size distributions of the pumice clasts suggest a complex history involving continuous and/or accelerating vesicle nucleation and growth, along with subsequent coalescence and collapse. The shift in eruption dynamics from a steady to an unsteady and back to a steady plume during the ~ 87 ka Baricha eruption is attributed to multiple factors, including changes in conduit geometry, abundance of lithics in the eruptive mixture, variations in decompression rate, and (cryptic) injection of fresh magma. These findings not only enhance our understanding of peralkaline eruption dynamics but also contribute to improving the ability to forecast potential volcanic hazards. The implications extend beyond the East African Rift to benefit the study of other peralkaline rhyolite volcanoes worldwide.

Supplementary Information The online version contains supplementary material available at https://doi.org/10.1007/s00445-024-01787-9.

Acknowledgements Field work in ethiopia was permited by authorities of the Oromia regional state, and professional logistical support was provided by Ethioder Pvt Ltd co. Our gratitude goes to Natalia Pardo for editorial handling, and to Thomas Giachetti and Rebecca deGraffenried for their detailed and constructive comments, which significantly improved the paper.

Funding AT was supported by a Fonds National de la Recherche Scientifique (F.R.S.-FNRS) Aspirant doctoral scholarship, and a Wiener-Anspach Foundation (FWA) postdoctoral fellowship. KF acknowledges support from the Wiener-Anspach Foundation and FNRS MIS grant F.4515.20F, as well as Natural Environment Research Council large grant NE/L013932/1 (RiftVolc) during which some of the foundations of this work were initiated. PW acknowledges support from an F.R.S.-FNRS postdoctoral research fellowship, as well as LMUexcellent, funded by the Federal Ministry of Education and Research (BMBF) and the Free State of Bavaria under the Excellence Strategy of the Federal Government and the Länder. LG acknowledges the Laboratory of Excellence ClerVolc contribution number 665.

Data availability All data utilized in this manuscript are provided in the supplementary information.

Declarations

Conflict of interest The authors declare no competing interests.

References

Agostini A, Bonini M, Corti G, Sani F, Manetti P (2011) Distribution of quaternary deformation in the central Main Ethiopian Rift, East Africa. Tectonics 30(4). https://doi.org/10.1029/2010TC002833

Alfano F, Bonadonna C, Gurioli L (2012) Insights into eruption dynamics from textural analysis: the case of the May, 2008, Chaitén eruption. Bull Volcanol 74:2095–2108

Bizouard H, Di Paola GM (1978) Mineralogy of the Tullu Moje active volcanic area (Arussi: Ethiopian Rift valley). In: Petrology and geochemistry of continental rifts. Springer, Dordrecht, pp 87–100

Blott SJ, Pye K (2008) Particle shape: a review and new methods of characterization and classification. Sedimentology 55(1):31–63

Blower JD, Keating JP, Mader HM, Phillips JC (2003) The evolution of bubble size distributions in volcanic eruptions. J Volcanol Geoth Res 120(1–2):1–23

Bonadonna C, Costa A (2013) Plume height, volume, and classification of explosive volcanic eruptions based on the Weibull function. Bull Volcanol 75:1–19

Bonadonna C, Cioni R, Pistolesi M, Connor C, Scollo S, Pioli L, Rosi M (2013) Determination of the largest clast sizes of tephra deposits for the characterization of explosive eruptions: a study of the IAVCEI commission on tephra hazard modelling. Bull Volcanol 75:1–15

Cáceres F, Wadsworth FB, Scheu B, Colombier M, Madonna C, Cimarelli C, Hess K, Kaliwoda M, Ruthensteiner B, Dingwell DB (2020) Can nanolites enhance eruption explosivity? Geology 48(10):997–1001

Campagnola S, Romano C, Mastin LG, Vona A (2016) Confort 15 model of conduit dynamics: applications to Pantelleria Green Tuff and Etna 122 BC eruptions. Contrib Miner Petrol 171:1–25

Carey S, Sparks RSJ (1986) Quantitative models of the fallout and dispersal of tephra from volcanic eruption columns. Bull Volcanol 48:109–125

Carey RJ, Houghton BF, Thordarson T (2009) Abrupt shifts between wet and dry phases of the 1875 eruption of Askja Volcano: microscopic evidence for macroscopic dynamics. J Volcanol Geoth Res 184(3–4):256–270

Carey S, Bursik M (2015) Volcanic plumes. In: The encyclopedia of volcanoes. Academic Press, pp 571–585. https://doi.org/10.1016/B978-0-12-385938-9.00032-8

Cas R, Wright J (1987) Volcanic successions, modern and ancient: a geological approach to processes, products and successions. Unwin Hyman Ltd, London

Cashman KV, Scheu B (2015) Magmatic fragmentation. In: The encyclopedia of volcanoes. Academic Press, pp 459–471. https://doi.org/10.1016/B978-0-12-385938-9.00025-0

Cassidy M, Manga M, Cashman K, Bachmann O (2018) Controls on explosive-effusive volcanic eruption styles. Nat Commun 9(1):2839

Castro JM, Dingwell DB (2009) Rapid ascent of rhyolitic magma at Chaitén volcano, Chile. Nature 461(7265):780–783

Castro JM, Cordonnier B, Tuffen H, Tobin MJ, Puskar L, Martin MC, Bechtel HA (2012) The role of melt-fracture degassing in defusing explosive rhyolite eruptions at volcán Chaitén. Earth Planet Sci Lett 333:63–69

Cioni R, D'Oriano C, Bertagnini A (2008) Fingerprinting ash deposits of small scale eruptions by their physical and textural features. J Volcanol Geoth Res 177(1):277–287

Cioni R, Pistolesi M, Rosi M (2015) Plinian and subplinian eruptions. In: The encyclopedia of volcanoes. Academic Press, pp 519–535. https://doi.org/10.1016/B978-0-12-385938-9.00029-8

Clarke B, Calder ES, Dessalegn F, Fontijn K, Cortés JA, Naylor M, Butler I, Hutchison W, Yirgu G (2019) Fluidal pyroclasts reveal the intensity of peralkaline rhyolite pumice cone eruptions. Nat Commun 10(1):2010

Colby DJ, Pyle DM, Fontijn K, Mather TA, Melaku AA, Mengesha MA, Yirgu G (2022) Stratigraphy and eruptive history of Corbetti Caldera in the Main Ethiopian Rift. J Volcanol Geoth Res 428:107580

Colombier M, Wadsworth FB, Gurioli L, Scheu B, Kueppers U, Di Muro A, Dingwell DB (2017a) The evolution of pore connectivity in volcanic rocks. Earth Planet Sci Lett 462:99–109

Colombier M, Gurioli L, Druitt TH, Shea T, Boivin P, Miallier D, Cluzel N (2017b) Textural evolution of magma during the 9.4-ka trachytic explosive eruption at Kilian Volcano, Chaîne des Puys. France Bulletin of Volcanology 79:1–24

Degruyter W, Huber C, Bachmann O, Cooper KM, Kent AJ (2016) Magma reservoir response to transient recharge events: the case of Santorini volcano (Greece). Geology 44(1):23–26

Di Paola GM (1972) The Ethiopian Rift Valley (between 7 00′ and 8 40′ lat. north). Bull Volcanol 36(4):517–560

Di Genova D, Romano C, Hess KU, Vona A, Poe BT, Giordano D, Dingwell DB, Behrens H (2013) The rheology of peralkaline rhyolites from Pantelleria Island. J Volcanol Geoth Res 249:201–216

Dingwell DB, Hess KU, Romano C (1998) Extremely fluid behavior of hydrous peralkaline rhyolites. Earth Planet Sci Lett 158(1–2):31–38

Dingwell DB, Lavallée Y, Hess KU, Flaws A, Marti J, Nichols AR, Gilg HA, Schillinger B (2016) Eruptive shearing of tube pumice: pure and simple. Solid Earth 7(5):1383–1393

Fontijn K, McNamara K, Tadesse AZ, Pyle DM, Dessalegn F, Hutchison W, Mather TA, Yirgu G (2018) Contrasting styles of post-caldera volcanism along the Main Ethiopian Rift: implications for contemporary volcanic hazards. J Volcanol Geoth Res 356:90–113

Gaonac'h H, Lovejoy S, Stix J, Scherzter D (1996) A scaling growth model for bubbles in basaltic lava flows. Earth Planet Sci Lett 139(3–4):395–409

Gardner JE, Thomas RM, Jaupart C, Tait S (1996) Fragmentation of magma during Plinian volcanic eruptions. Bull Volcanol 58:144–162

Giachetti T, Druitt TH, Burgisser A, Arbaret L, Galven C (2010) Bubble nucleation, growth and coalescence during the 1997 Vulcanian explosions of Soufrière Hills Volcano, Montserrat. J Volcanol Geoth Res 193(3–4):215–231

Gurioli L, Houghton BF, Cashman KV, Cioni R (2005) Complex changes in eruption dynamics during the 79 AD eruption of Vesuvius. Bull Volcanol 67:144–159

Gurioli L, Andronico D, Bachèlery P, Balcone-Boissard H, Battaglia J, Boudon G, Burgisser A, Burton MR, Cashman K, Cichy S, Cioni R, Di Muro A, Dominguez L, D'Oriano C, Druitt T, Harris AJL, Hort M, Kelfoun K, Komorowski JC, Kueppers U, Le Pennec JL, Menand T, Paris R, Pioli L, Pistolesi M, Polacci M, Pompilio M, Ripepe M, Roche O, Rose-Koga E, Rust A, Schiavi F, Scharff L, Sulpizio R, Taddeucci J, Thordarson T (2015) MeMoVolc consensual document: a review of cross-disciplinary approaches to characterizing small explosive magmatic eruptions. Bull Volcanol 77:1–33

Houghton BF, Wilson CJN (1989) A vesicularity index for pyroclastic deposits. Bull Volcanol 51(6):451–462

Houghton BF, Carey RJ, Cashman KV, Wilson CJ, Hobden BJ, Hammer JE (2010) Diverse patterns of ascent, degassing, and eruption of rhyolite magma during the 1.8 ka Taupo eruption, New Zealand: evidence from clast vesicularity. J Volcanol Geotherm Res 195(1):31–47

Houghton B, Carey RJ (2015) Pyroclastic fall deposits. In: The encyclopedia of volcanoes. Academic Press, pp 599–616. https://doi.org/10.1016/B978-0-12-385938-9.00034-1

Hughes EC, Neave DA, Dobson KJ, Withers PJ, Edmonds M (2017) How to fragment peralkaline rhyolites: observations on pumice using combined multi-scale 2D and 3D imaging. J Volcanol Geoth Res 336:179–191

Iddon F, Edmonds M (2020) Volatile-rich magmas distributed through the upper crust in the Main Ethiopian Rift. Geochem Geophys Geosyst 21(6):e2019GC008904

Iddon F, Jackson C, Hutchison W, Fontijn K, Pyle DM, Mather TA, Yirgu G, Edmonds M (2019) Mixing and crystal scavenging in the Main Ethiopian Rift revealed by trace element systematics in feldspars and glasses. Geochem Geophys Geosyst 20(1):230–259

Inman DL (1952) Measures for describing the size distribution of sediments. J Sediment Res 22(3):125–145

Kent AJ, Till CB, Cooper KM (2023) Start me up: the relationship between volcanic eruption characteristics and eruption initiation mechanisms. Volcanica 6(2):161–172

Klug C, Cashman KV (1996) Permeability development in vesiculating magmas: implications for fragmentation. Bull Volcanol 58(2):87–100

Klug C, Cashman KV, Bacon C (2002) Structure and physical characteristics of pumice from the climactic eruption of Mount Mazama (Crater Lake), Oregon. Bull Volcanol 64:486–501

Marti J, Soriano C, Dingwell DB (1999) Tube pumices as strain markers of the ductile–brittle transition during magma fragmentation. Nature 402(6762):650–653

McCartney KN, Hammer JE, Shea T, Brachfeld S, Giachetti T (2024) Evaluating the role of titanomagnetite in bubble nucleation: novel applications of low temperature magnetic analysis and textural characterization of rhyolite pumice and obsidian from Glass Mountain, California. Geochem Geophys Geosyst 25(4):e2023GC011338

Pardo N, Cronin SJ, Wright HM, Schipper CI, Smith I, Stewart B (2014) Pyroclast textural variation as an indicator of eruption column steadiness in andesitic Plinian eruptions at Mt. Ruapehu. Bull Volcanol 76:1–19

Pistolesi M, Cioni R, Bonadonna C, Elissondo M, Baumann V, Bertagnini A, Chiari L, Gonzales R, Rosi M, Francalanci L (2015) Complex dynamics of small-moderate volcanic events: the example of the 2011 rhyolitic Cordón Caulle eruption, Chile. Bull Volcanol 77:1–24

Polacci M, Papale P, Rosi M (2001) Textural heterogeneities in pumices from the climactic eruption of Mount Pinatubo, 15 June 1991, and implications for magma ascent dynamics. Bull Volcanol 63:83–97

Polacci M, Pioli L, Rosi M (2003) The Plinian phase of the Campanian Ignimbrite eruption (Phlegrean Fields, Italy): evidence from

density measurements and textural characterization of pumice. Bull Volcanol 65(6):418–432
Rossi E, Bonadonna C, Degruyter W (2019) A new strategy for the estimation of plume height from clast dispersal in various atmospheric and eruptive conditions. Earth Planet Sci Lett 505:1–12
Ruprecht P, Bachmann O (2010) Pre-eruptive reheating during magma mixing at Quizapu volcano and the implications for the explosiveness of silicic arc volcanoes. Geology 38(10):919–922
Rust AC, Cashman KV (2011) Permeability controls on expansion and size distributions of pyroclasts. J Geophys Res Solid Earth 116(B11). https://doi.org/10.1029/2011JB008494
Sahagian DL, Proussevitch AA (1998) 3D particle size distributions from 2D observations: stereology for natural applications. J Volcanol Geoth Res 84(3–4):173–196
Schneider CA, Rasband WS, Eliceiri KW (2012) NIH Image to ImageJ: 25 years of image analysis. Nat Methods 9(7):671–675
Shamloo HI, Grunder AL (2023) Magma mingling and ascent in the minutes to hours before an explosive eruption as recorded by banded pumice. Geology 51(10):957–961
Shea T (2017) Bubble nucleation in magmas: a dominantly heterogeneous process? J Volcanol Geoth Res 343:155–170
Shea T, Houghton BF, Gurioli L, Cashman KV, Hammer JE, Hobden BJ (2010) Textural studies of vesicles in volcanic rocks: an integrated methodology. J Volcanol Geoth Res 190(3–4):271–289
Shea T, Gurioli L, Houghton BF, Cioni R, Cashman KV (2011) Column collapse and generation of pyroclastic density currents during the AD 79 eruption of Vesuvius: the role of pyroclast density. Geology 39(7):695–698
Shea T, Gurioli L, Houghton BF (2012) Transitions between fall phases and pyroclastic density currents during the AD 79 eruption at Vesuvius: building a transient conduit model from the textural and volatile record. Bull Volcanol 74:2363–2381
Shea T, Hellebrand E, Gurioli L, Tuffen H (2014) Conduit-to localized-scale degassing during Plinian eruptions: insights from major element and volatile (Cl and H_2O) analyses within Vesuvius AD 79 pumice. J Petrol 55(2):315–344
Sparks SR, Sigurdsson H, Wilson L (1977) Magma mixing: a mechanism for triggering acid explosive eruptions. Nature 267:315–318
Tadesse AZ, Ayalew D, Pik R, Yirgu G, Fontijn K (2019) Magmatic evolution of the Boku volcanic complex, Main Ethiopian Rift. J Afr Earth Sc 149:109–130
Tadesse AZ, Fontijn K, Melaku AA, Gebru EF, Smith VC, Tomlinson E, Barford D, Gopon P, Bégué F, Caricchi L, Laha P, Yirgu G, Ayalew D (2022) Eruption frequency and magnitude in a geothermally active continental rift: the Bora-Baricha-Tullu Moye volcanic complex, Main Ethiopian Rift. J Volcanol Geoth Res 423:107471
Tadesse AZ, Bedassa G, Kervyn M, Muluneh AA, Gudbrandsson S, Yirgu G, Ayalew D, Fontijn K (2023a) Structural controls on magma pathways in Bora-Baricha-Tullu Moye (BBTM) volcanic system, Main Ethiopian Rift. Volcanica 6(2):367–390
Tadesse AZ, Fontijn K, Caricchi L, Bégué F, Gudbrandsson S, Smith VC, Gopon P, Debaille V, Laha P, Terryn H, Yirgu G, Ayalew D (2023b) Pre-eruptive storage conditions and magmatic evolution of the Bora-Baricha-Tullu Moye volcanic system, Main Ethiopian Rift. Lithos:107088. https://doi.org/10.1016/j.lithos.2023.107088
Tait S, Jaupart C, Vergniolle S (1989) Pressure, gas content and eruption periodicity of a shallow, crystallising magma chamber. Earth Planet Sci Lett 92(1):107–123
Tait S, Thomas R, Gardner J, Jaupart C (1998) Constraints on cooling rates and permeabilities of pumice in an explosive eruption jet from colour and magnetic mineralogy. J Volcanol Geoth Res 86(1–4):79–91
Thomas RME, Sparks RSJ (1992) Cooling of tephra during fallout from eruption columns. Bull Volcanol 54(7):542–553
Toramaru A (1989) Vesiculation process and bubble size distributions in ascending magmas with constant velocities. J Geophys Res Solid Earth 94(B12):17523–17542
Toramaru A (2006) BND (bubble number density) decompression rate meter for explosive volcanic eruptions. J Volcanol Geoth Res 154(3–4):303–316
Walker GP (1971) Grain-size characteristics of pyroclastic deposits. J Geol 79(6):696–714
Wilson L, Sparks RSJ, Walker GP (1980) Explosive volcanic eruptions—IV. The control of magma properties and conduit geometry on eruption column behaviour. Geophys J Int 63(1):117–148
WoldeGabriel G, Aronson JL, Walter RC (1990) Geology, geochronology, and rift basin development in the central sector of the Main Ethiopia Rift. Geol Soc Am Bull 102(4):439–458
Zimanowski B, Büttner R, Dellino P, White JD, Wohletz KH (2015) Magma–water interaction and phreatomagmatic fragmentation. In: The encyclopedia of volcanoes. Academic Press, pp 473–484. https://doi.org/10.1016/B978-0-12-385938-9.00026-2